Alcohols Enrichment Enables Their Electrooxidation Coupled with H_2 Production at High Current Density

Zhenhua Li
Beijing University of Chemical Technology
Yifan Yan
Beijing University of Chemical Technology
Si-Min Xu
State Key Laboratory of Chemical Resource Engineering, Beijing Advanced Innovation Centre for Soft Matter Science and Engineering, Beijing University of Chemical Technology
Hua Zhou
Tsinghua University
Ming Xu
Beijing University of Chemical Technology
Lina Ma
Beijing University of Chemical Technology
Xianggui Kong
Beijing University of Chemical Technology
Bin Wang
Beijing Research Institute of Chemical Industry, Sinopec Group
Lirong Zheng
Chinese Academy of Sciences
Haohong Duan (hhduan@mail.tsinghua.edu.cn)
Tsinghua University https://orcid.org/0000-0003-3210-0068

Article

Keywords: Electrochemical alcohols oxidation, H2 production, high current density

Posted Date: December 28th, 2020

DOI: https://doi.org/10.21203/rs.3.rs-119270/v1

Abstract

Electrochemical alcohols oxidation offers a promising approach to produce industrial-relevant chemicals and facilitate coupled H_2 production. However, the corresponding current density is very low at moderate cell potential that substantially limits the overall productivity. Here, we report enrichment of alcohols in local environment over a cooperative catalyst of Au nanoparticles supported on cobalt oxyhydroxide nanosheets (Au/CoOOH), enabling alcohols electrooxidation at high current density. Specifically, the current density of benzyl alcohol electrooxidation can reach 523 mA cm^{-2} at potential of 1.5 V vs. RHE. Experimental and theoretical results suggest that benzyl alcohol molecules are enriched on Au/CoOOH interface via strong d-π interaction. The enrichment has a broad substrate scope that involves alcohols with α-π bond including α-phenyl, C = C and C = O groups. Based on these findings, we design an intermittent potential (IP) strategy for long-term alcohol enrichment, achieving electrooxidation with current density of > 250 mA cm^{-2} over 24 hours and promoted productivity.

Introduction

Hydrogen (H_2) is a promising energy to replace fossil fuels that addresses the environmental problems associated with global warming and alleviates the energy crisis. Electrocatalytic water splitting powered by clean energy (*e.g.*, solar energy, wind) represents a green approach to produce H_2[1,2]. However, this process still suffers from large overall electricity consumption stemming from high cell potential due to the sluggish four-electron transfer of anodic oxygen evolution reaction (OER)[3,4]. Developing anodic reactions with cell potential lower than OER could be a promising strategy for fundamentally lowering the energy requirements for electrocatalytic H_2 production. Such anode oxidation reactions have additional benefit of producing high value-added chemicals from inexpensive industrial byproducts or renewable biomass carbon sources[5,6]. For reactions of this kind, large positive potential unavoidably results in uncontrolled OER, therefore applying moderate potential is necessary to achieve high Faradaic efficiency (FE) toward target products[7]. Tremendous efforts have been devoted to developing electrocatalysts with improved catalytic activities[8–13]. Despite these efforts, the reported current density remains very low under moderate cell potential, such as the electrooxidation of alcohols[8,9], 5-hydroxymethyfurfural (HMF)[10,11], primary amines[12] and tetrahydroisoquinolines[13] are often operated at current density lower than 200 mA cm^{-2}. The production of relevant target chemicals coupled with H_2 evolution at low current density would hamper the overall efficiency for industrial production.

Among the value-added anodic reactions, alcohol oxidation reactions (AORs) are particularly important for their wide applications in commodity chemicals production[14]. For instance, oxidation of benzyl alcohol produces benzoic acid, which is an important fine chemical used in synthetic fiber, resin, and antiseptic industries[15]. Oxidation of polyols (such as glycerol) afford corresponding ketones/aldehydes and formate, which can find applications as degradable plastic monomer, dyestuffs and food additives[16–18]. However, their large-scale productions using electrochemical approach have yet to be realized because of the insufficient productivity derived from the low current density. One of the limitations might be the low

alcohol concentration in the vicinity of the catalytically active sites at anode that hinders reaction occurring (Scheme 1a; Typically, water is used as the electrolyte for good alcohol solubility). In line with this rationale, enriching alcohol molecules at the anode *via* electrocatalyst surface engineering would possibly promote alcohol oxidation productivity, but this strategy has rarely been considered.

For electrocatalytic reaction of gaseous molecules, for instance, CO_2, N_2 and CH_4, it has been demonstrated that constructing a hydrophobic surface on the electrode is beneficial to their enrichment and therefore facilitate the reactivity[19–21]. However, this strategy may not be applicable for electrooxidation of alcohols often featuring hydrophilic property. Very recently, Sargent *et al.* reported porphyrin-based metallic complexes on metal electrode as adsorption sites for CO, a key intermediate during CO_2 reduction, thus increasing CO concentration on the electrode and achieving ethanol generation with high rate and selectivity[19]. Inspired by the catalyst design principle, we hypothesize that constructing adsorption site for alcohol on the AOR-active anode would increase local alcohol concentration and thereby promote the current density of AOR coupled with H_2 generation.

Herein, we report the enrichment of alcohols in local environment by synthesizing a cooperative catalyst of Au nanoparticles supported on cobalt oxyhydroxide nanosheets (Au/CoOOH), which greatly enhances the current density in electrocatalytic oxidation of alcohols coupled with H_2 production (Scheme 1b). Specifically, the Au/CoOOH exhibits current density of 330 mA cm^{-2} at potential of 1.3 V *vs.* RHE in 1 M KOH with 0.1 M benzyl alcohol at room temperature (r.t.). The benzyl alcohol oxidation rate delivers 3.19 mmol cm^{-2} h^{-1} (corresponding to 968 C cm^{-2} h^{-1}), which is 50 and 17-fold higher than that of CoOOH and Au samples, respectively. The coupled cathodic H_2 production rate reaches 54 and 19-fold enhancement than CoOOH and Au, respectively. The current density could further reach 523 mA cm^{-2} at 1.5 V *vs.* RHE. *In-situ* infrared spectroscopy combined with density functional theory (DFT) calculations and *ab initio* molecular dynamics (AIMD) simulations demonstrate that benzyl alcohol molecules can be strongly adsorbed on the Au/CoOOH interface *via d-π* interaction between the *d* orbital of Au and *π** orbital of benzyl alcohol, together with the hydrogen bonding between the surface terminated O of CoOOH and hydroxyl group of benzyl alcohol, leading to the enrichment of benzyl alcohol in local environment. The Au/CoOOH catalyst is also efficient to enrich diverse alcohols with *α*-π bond consisting of *α*-phenyl, C = C and C = O groups with 2 ~ 20-fold higher electrooxidation rate than CoOOH. We found that while Au gradually gets oxidized at anodic potential, it can readily undergo reduction at open circuit with revival of the enrichment ability. Based on these findings, by deploying an intermittent potential (IP) strategy between anodic potential and open circuit, we achieve long-term alcohol enrichment, maintaining high current density (> 250 mA cm^{-2} at 1.35 V *vs.* RHE) for benzyl alcohol electrooxidation over 24 h. As a result, the productivities of oxidation products (benzaldehyde and benzoic acid) and H_2 achieved 10- and 9-fold increment compared with constant potential (CP) strategy, together with electric energy saving of 43 and 33% at 200 and 300 mA cm^{-2}, respectively.

Results

Catalyst synthesis and characterizations. The cooperative catalyst of Au nanoparticles supported on CoOOH nanosheets (Au/CoOOH) was prepared *via* a two-step electrochemical method, in which $Co(OH)_2$ was initially synthesized on nickel (Ni) foam, then Au nanoparticles were electrodeposited onto $Co(OH)_2$. The as-prepared $Au/Co(OH)_2$ was electro-oxidized in 1 M KOH solution to structurally transform to Au/CoOOH. For catalytic comparison, CoOOH nanosheets and Au nanoparticles on Ni foam were also synthesized following similar methods. Scanning electron microscope (SEM) images (Fig. 1a and Supplementary Fig. 1) show that the as-synthesized Au/CoOOH nanosheets (with an average thickness of ~10 nm and diameter of 200–300 nm) are vertically grown on Ni foam and form array structure. High-resolution transmission electron microscope (HRTEM) images reveal that Au nanoparticles are well dispersed on the CoOOH nanosheets (Fig. 1b and supplementary Fig. 2) with average diameter of 4.3 nm (Fig. 1c). The HRTEM image of an individual Au nanoparticle displays fringe distances of 0.203 nm (Fig. 1b; inset), closely matching the (200) plane of face-centered-cubic Au. X-ray diffraction (XRD) analysis of $Au/Co(OH)_2$ and Au/CoOOH reveals a typical structure transformation from α-$Co(OH)_2$ to γ-CoOOH phase because the (003) diffraction peak shifts from 10.1° to 12.9° (Fig. 1d and Supplementary Fig. 3)[22,23], together with the sharp peaks from Ni foam substrate. The Au (111) reflection at $2\theta = 38.2°$ for both $Au/Co(OH)_2$ and Au/CoOOH is very weak due to the small size of Au nanoparticles. Inductively coupled plasma-atomic emission spectrometry (ICP-AES) confirms that the mass loading of Au on CoOOH was 11.3 wt% (Supplementary Table 1).

Benzyl alcohol electrooxidation. Electrochemical oxidation of benzyl alcohol was tested to evaluate the catalytic performance of Au/CoOOH. Au and CoOOH were used as the reference catalysts. Fig. 2a shows their linear sweep voltammetry (LSV) curves. The CoOOH exhibits an onset potential of ~1.48 V *vs*. RHE for water oxidation in 1 M KOH solution. After adding 0.1 M benzyl alcohol, the onset potential is reduced to ~1.28 V *vs*. RHE, in consistent with previous report[24]. Although the current density increases compared with OER process, it is still very low at moderate cell voltage (only 19 and 53 mA cm^{-2} at 1.3 and 1.4 V *vs*. RHE, respectively). As for Au catalyst, the current density starts to decay rapidly from ~1.35 V *vs*. RHE, which is due to Au deactivation as reported for noble metal catalysis[25–28]. Notably, by using Au/CoOOH as the catalyst, the onset potential shifts negatively to ~1.0 V *vs*. RHE with significant enhancement of current density compared with CoOOH (from 19 to 330 mA cm^{-2} at 1.3 V *vs*. RHE based on the LSV curves). The current density further reaches 439 and 523 mA cm^{-2} at moderate potential of 1.4 and 1.5 V *vs.* RHE, respectively. To the best of our knowledge, these current density values are the highest reported so far for electrocatalytic AORs (Fig. 2b and Supplementary Table 2)[29–34].

Chronoamperometric (CA) measurement was then carried out. As shown in Fig. 2c, the current-time (*I*-*t*) curve of Au/CoOOH shows a high initial current density of ~330 mA cm^{-2}

at 1.3 V *vs*. RHE in 1 M KOH with 0.1 M benzyl alcohol at r.t., much higher than that of CoOOH (with an initial current density of ~20 mA cm^{-2}). Although the Au catalyst exhibits an initial current density of 152 mA cm^{-2}, it decays rapidly to lower than 6 mA cm^{-2} within 600 s. In addition, the current densities are very weak in the absence of benzyl alcohol (Supplementary Fig. 4), indicating that the high current density over Au/CoOOH is caused by the oxidation of the benzyl alcohol, rather than the reduction of Co, OH^- adsorption or other effects on the surface.

Fig. 2d shows the benzyl alcohol conversion rate (left column), space-time yield of H_2 and Faradaic efficiency (FE) (right column) over different catalysts. The conversion rate for benzyl alcohol oxidation over Au/CoOOH reaches 3.19 mmol cm^{-2} h^{-1} (corresponding to 968 C cm^{-2} h^{-1}) with FE of 99% at 1.3 V *vs*. RHE (Fig. 1e), which is 50 and 17-fold higher than that of CoOOH and Au, respectively. The kinetic curves for benzyl alcohol conversion as function of reaction time reveals its sequential oxidation to benzaldehyde and then to benzoic acid is involved (Supplementary Fig. 5). As for the H_2 production at the counterpart Pt cathode, the space-time yield reaches 117.9 mL cm^{-2} h^{-1} when Au/CoOOH is used as the anode, significantly higher than CoOOH (2.2 mL cm^{-2} h^{-1}) and Au (6.1 mL cm^{-2} h^{-1}).

Mechanistic investigation of benzyl alcohol enrichment. To study the current density enhancement for benzyl alcohol electrooxidation over Au/CoOOH, *in-situ* Fourier transformed infrared (FTIR) spectroscopy was conducted to study the interaction between benzyl alcohol and the catalyst. Benzyl alcohol molecule in gas phase shows typical skeletal vibration of the benzene ring at 1455 cm^{-1}, δ(O−H) at 1209 cm^{-1} and ν(C−O) at 1022 cm^{-1} (Supplementary Fig. 6) [35–37]. When benzyl alcohol was adsorbed on CoOOH, the peak positions are close to gaseous benzyl alcohol, and it was easily removed by He purging within 15 min (Fig. 3a), indicating benzyl alcohol is weakly adsorbed on CoOOH[38]. As for benzyl alcohol adsorbed on Au/CoOOH, the band intensity that corresponds to skeletal vibration of the benzene ring (peak at 1455 cm^{-1}) decreases considerably and widens towards lower wavenumber, together with the appearance of new bands at around 1435 and 1418 cm^{-1} (Fig. 3b). These variations may be attributed to the interaction between Au and benzene ring of benzyl alcohol that leads to the decrease of benzene symmetry, because breaking of symmetry was demonstrated to give rise to band shifting and splitting[39]. Moreover, the bands of δ(O−H) and ν(C−O) shift to lower wavenumbers and the intensity of δ(O−H) band is weakened due to the adsorption of benzyl alcohol[40,41]. New bands at 1125 cm^{-1} were observed, which are assigned to the stretching mode of C−O bond of alcoholate species adsorbed on the CoOOH[42]. Importantly, the signals of adsorbed benzyl alcohol maintained over 20 min of He purging, indicating a strong interaction exists between benzyl alcohol and Au/CoOOH.

To understand the enhanced adsorption of benzyl alcohol on Au/CoOOH, spin-polarized DFT calculations were carried out. Three models were constructed to represent CoOOH surface, Au surface and Au/CoOOH interface in Au/CoOOH, denoted as CoOOH, Au, and Au/CoOOH, respectively (Supplementary Fig. 7). The calculated adsorption energy of benzyl alcohol is much lower on Au/CoOOH (Fig. 3c), suggesting that the adsorption of benzyl alcohol on Au/CoOOH is thermodynamically more preferable. By analyzing the density of states and Hirshfeld charge of Au/CoOOH, together with the frontier orbitals of benzyl alcohol, it can be deduced that the electron in occupied Au 5*d* orbital can transfer to the unoccupied π^* orbital of benzyl alcohol (Fig. 3d, Supplementary Fig. 8a and Supplementary Note 1)[43]. This *d*-π interaction endows Au/CoOOH with stronger adsorption ability to benzyl alcohol than CoOOH. Meanwhile, the interaction between hydroxyl group of benzyl alcohol and terminated-O on CoOOH *via* hydrogen bonding also contributes to the enhanced adsorption energy (Supplementary Fig. 8b).

To consider the enrichment of benzyl alcohol on Au/CoOOH in real reaction system, AIMD simulations were performed by positioning Au/CoOOH in a solvent box filled with water (the electrolyte in reaction) and four benzyl alcohol molecules (denoted as Au/CoOOH_sol). The adsorption of benzyl alcohols on CoOOH was also simulated under the same conditions for comparison (denoted as CoOOH_sol). As displayed in Fig. 3e and Supplementary video 1 and 2, after simulation time of 1000 ps, only one benzyl alcohol molecule was adsorbed on CoOOH, while the other three remained in the bulk solution. For Au/CoOOH_sol, all of the molecules approached to and then were enriched on Au/CoOOH surface within 200 ps (Fig. 3f). After total simulation time of 1000 ps, three of the molecules were finally adsorbed on Au/CoOOH interface, and another one on Au surface. During the adsorption process, the total energy of Au/CoOOH_sol decreased, while there was no obvious decrease for CoOOH_sol (Fig. 3g). These results suggest the possibility of Au/CoOOH for benzyl alcohol enrichment in real reaction system, and the interface between Au and CoOOH is the preferential adsorption site.

To understand the reaction mechanism of benzyl alcohol oxidation, Gibbs free energy diagrams of benzyl alcohol oxidation to benzoic acid were calculated over different catalysts (Fig. 4a; Supplementary Figs. 9-11, Table 3 and Note 2). The reaction begins with benzyl alcohol adsorption, then it is oxidized to benzaldehyde and finally to benzoic acid. For CoOOH and Au catalysts, the rate-determining step (RDS) is the benzaldehyde formation, with the reaction barrier of 1.45 and 1.34 eV, respectively. Due to the strong *d*-π interaction, the energy of adsorbed benzaldehyde (Ph-CHO*) is decreased on Au/CoOOH, thus lowering the Gibbs free energy barrier for the benzaldehyde formation step to 1.09 eV. The RDS over Au/CoOOH in turn switches to the generation of benzoic acid with lower reaction barrier (1.26 eV) compared with CoOOH and Au. To consider the real reaction system wherein more benzyl alcohol molecules may cover on the catalyst as indicated by AIMD results, the calculation of Gibbs free energy diagrams was investigated in the presence of five benzyl alcohol molecules adsorbed on the Au/CoOOH interface (see

Supplementary Fig. 12). As shown in Fig. 4b, the resulting reaction barrier of RDS (benzyl alcohol to benzoic acid) is lower than the case of one molecule, indicating that benzyl alcohol oxidation is easier to proceed when more molecules are enriched on Au/CoOOH.

Substrate scoping. To demonstrate the general applicability of the alcohol enrichment over Au/CoOOH catalyst, benzyl alcohols with diverse substituents (−Cl, −F, $-CH_3$, $-CF_3$, $-OCH_3$, $-C(CH_3)_3$) were examined. The electrooxidations were performed at 60 ºC to guarantee alcohols dissolution in 1 M KOH. The catalytic results show that the Au/CoOOH exhibits 2 to 16-fold enhancement of current density (representing as charge transfer) compared with CoOOH, together with higher production rates of alcohol-oxidized products (entries 1-6, Table 1; and Supplementary Fig. 13) and comparably high FE towards them. Among these alcohol molecules, benzyl alcohol substituted with $-C(CH_3)_3$ shows inferior activity (entry 6, Table 1), which may be due to the steric hindrance that inhibits benzene ring adsorption on Au/CoOOH. We further investigated the effect of phenyl and hydroxyl groups and their proximity on the current density. As shown in Supplementary Fig. 14, there is no current density enhancement for alcohols without phenyl group (ethanol and cyclohexanemethanol) or aromatics without hydroxyl group (toluene), suggesting the importance of hydroxyl and phenyl groups in benzyl alcohol for current density enhancement over Au/CoOOH. Moreover, we found that the Au/CoOOH shows very weak current density enhancement for alcohol without *α*-phenyl group (*β*-phenethyl alcohol; entry 7, Table 1), which is attributed to the relatively weak adsorption of *β*-phenethyl alcohol on Au/CoOOH demonstrated by DFT calculation (Supplementary Fig. 15).

To broaden the substrate scope, we explored the alcohols with *α*-C=C (methallyl alcohol) and *α*-C=O group (hydroxyacetone), because these groups contain *π* bond that resembles benzene ring. To our delight, Au/CoOOH catalyst exhibits higher current density and product yields for electrooxidation of these alcohols compared with CoOOH (entries 8 and 9, Table 1; and Supplementary Fig. 16). This can be explained by the calculated negative adsorption energies for their adsorption on Au/CoOOH, which is due to the strong interaction between *α*-C=C/-C=O groups and Au *via* Au(*d*)-*π* interaction (see Supplementary Fig. 17 and Supplementary Note 3). Furthermore, we found that the Au/CoOOH catalyst shows enhanced current density as well as higher product yields for electrooxidation of polyols with vicinal hydroxyl groups, including ethylene glycol, 1,2-propanediol and glycerol (entries 10-12, Table 1; and Supplementary Fig. 18), among which glycerol is an important biomass derivative produced in large amount in biodiesel production. The enhancement can be explained by the oxidation of $-CH_2-OH$ to -C=O under the reaction conditions[16,17], which leads to a similar enrichment effect as in the case of alcohol with *α*-C=O group.

[Please see the supplementary files section to view table 1.]

Understanding of the decay and revival of current density. We found that the current density decays gradually during the electrooxidation of benzyl alcohol (Fig. 5a), indicating a

deactivation process may be involved. However, the initial high current density can be restored after potential cut-off for approximately 100 s at open circuit. To unveil the underlying mechanism for the decay and revival of current density, operando extended X-ray absorption fine structure spectroscopy was conducted (operando EXAFS). Fig. 5b shows the Au L_3-edge XANES spectra of Au/CoOOH when anodic potential and open circuit were alternatively applied in 1 M KOH with 0.1 M benzyl alcohol. These operations are denoted as potential ON and OFF, respectively. When potential ON (1.4 V *vs*. RHE), the white line intensity enhances gradually (from line_a to line_d), which is assigned to Au oxidation possibly by the electrolyte, as verified by operando Au L_3-edge XANES spectra (Supplementary Fig. 19). This process is accompanied by the gradual decay of current density, suggesting that Au oxidation may has a negative effect on alcohol enrichment. This was confirmed by pre-oxidizing Au/CoOOH prior to introducing benzyl alcohol into the electrolyte, which shows very low catalytic activity (Supplementary Fig. 20). Subsequently, potential OFF was exerted and it causes weakening of white line intensity (from line_d to line_f), indicating that Au is reduced at open circuit. It should be noted that Au cannot be reduced in 1 M KOH electrolyte alone (Supplementary Fig. 19), suggesting that Au is more likely reduced by benzyl alcohol. Indeed, alcohols can be used as reducing agent.[44,45] This process is accompanied by rapid revival of current density, suggesting that the reduced Au can again adsorb and enrich benzyl alcohol molecules. The Au oxidation/reduction processes was demonstrated reversible when further anodic potential (from line_f to line_i) and open circuit (from line_i to line_k) were applied (Fig. 5b), suggesting that we could readily regain the high current density by exerting potential OFF. It should be mentioned that Co species in Au/CoOOH is oxidized more rapidly compared with current density decay (Supplementary Fig. 21), suggesting that Co oxidation may not be the main reason for the current decay.

To investigate the structure of Au species in Au/CoOOH when it is oxidized or reduced, Fourier-transform Au L_3-edge EXAFS spectra was performed. As shown in Fig. 5c, the Au/CoOOH sample displays obvious Au−O bond in the *R*-space spectra under potential ON. Then, it is significantly weakened under potential OFF. This result indicates that the formation of Au-O(H) species under anodic potential could be the reason for the current decay, because Au-O(H) species can hinder the adsorption of benzyl alcohol on Au. We demonstrated the key role of Au in current density enhancement by using methionine as the poison reagent. As shown in Fig. 5d, the current density decays instantly when methionine was introduced to the electrolyte, which is attributed to the strong interaction between methionine and Au *via* Au-S bond that prevents benzyl alcohol from adsorption. The above results indicate that when Au gradually gets oxidized to form Au-O(H) species at anodic potential with attenuation of alcohol enrichment, it can reversibly undergo reduction at open circuit with revival of the enrichment ability (Fig. 5e).

Intermittent potential strategy. In light of the findings that the alcohol enrichment could be reversible, we sought to develop an intermittent potential (IP) strategy to maintain the high current density in long-term electrooxidation of benzyl alcohol over Au/CoOOH, *via* alternatively switching between anodic potential (potential ON) and open circuit (potential OFF). Specifically, the reaction was initially conducted at 1.35 V *vs*. RHE in 1 M KOH with 0.1 M benzyl alcohol to get high current density (~400 mA cm^{-2}). When the current density decays to <250 mA cm^{-2}, we cut off the potential for about 100 s to regain the benzyl alcohol enrichment. Then we switched the potential back to 1.35 V *vs*. RHE with the recovery of initial high current density. By repeating the above operations, the current density can be maintained at high level (250-400 mA cm^{-2}) over 24 h (Fig. 6a). In contrast, the current density of Au/CoOOH decays from 400 to 60 mA cm^{-2} within 2 h using traditional constant potential (CP) strategy. As a result, the Au/CoOOH with IP strategy exhibits larger benzyl alcohol consumption, higher productivities of benzaldehyde, benzoic acid and H_2, and comparably high FE of total anodic products (Fig. 6b). The Au/CoOOH maintains its original structure after the reaction (Supplementary Fig. 22), demonstrating its stability. The electric energy consumption using IP and CP strategies were also compared. The Au/CoOOH with the IP strategy requires much lower potential to reach the same current density (Fig. 6c), together with 33-43 % energy saving (Fig. 6d).

Discussion

In summary, we achieve the enrichment of alcohols in local environment to enable their electrooxidation coupled with H_2 production at high current density by using a cooperative Au/CoOOH catalyst. Experimental studies, DFT calculations and AIMD simulations together reveal that Au/CoOOH interface has a strong enrichment ability for benzyl alcohol that derives from *d*-*π* interaction between the *d* orbital of Au and *π** orbital of benzyl alcohol, together with hydrogen bonding between CoOOH and hydroxyl group of benzyl alcohol. The substrate can be applied to a wide range of alcohols with *α*-π bond including *α*-phenyl, C = C and C = O groups. Based on the finding that Au can be readily reduced at open circuit with enhanced alcohol adsorption ability, we design an intermittent potential (IP) strategy for alcohol electrooxidation, which achieves long-term alcohol enrichment and thus high current density and productivities, and an energy-saving process is realized. This work may open up a promising avenue for anodic reaction coupling H_2 production at high current density *via* engineering adsorption sites for substrate enrichment.

Methods

General information

Except noted, all chemicals were purchased and used without further purification.

Catalyst preparation

The Au nanoparticles supported on CoOOH nanosheet catalyst (Au/CoOOH) was prepared *via* a two-step electrochemical method, in which $Co(OH)_2$ nanosheets was initially grown on nickel (Ni) foam, then Au nanoparticles were electrodeposited onto $Co(OH)_2$. Subsequently, the as-synthesized $Au/Co(OH)_2$ was electro-oxidized in 1 M KOH solution to enable the structural transformation to Au/CoOOH.

Preparation of $Co(OH)_2$ nanosheets: The nickel foam (10 × 20 × 1.5 mm) was used as matrix for growing $Co(OH)_2$ nanosheets array. Initially, the nickel foam (10 × 20 × 1.5 mm) was sequentially washed with dilute HCl (1 M), ethanol, and deionized water (each for 10 min) to remove surficial oxides and contaminants. The electrosynthesis of $Co(OH)_2$ nanosheet array was carried out in a three-electrodes setup, using saturated calomel electrode (SCE) and Pt foil as reference and counter electrodes respectively. The growth of $Co(OH)_2$ nanosheets was performed at constant potential (-1.0 V *vs*. SCE) in aqueous $Co(NO_3)_2$ (0.15 M) electrolyte for 300 seconds. The potentiostatic deposition was carried out at a potential of -1.0 V *vs*. SCE. The resulting $Co(OH)_2$ nanosheet array was withdrawn and rinsed thoroughly with ethanol and distilled water[46].

Preparation of $Au/Co(OH)_2$: The electrochemical deposition of Au nanoparticles onto $Co(OH)_2$ was carried out in a three-electrode configuration as above described. Specifically, Au nanoparticles were deposited on $Co(OH)_2$ by stepping the potential to −0.6 V *vs.* SCE for 10 s, followed by stepping back to −0.2 V *vs.* SCE for 10 s for three cycles, using aqueous electrolyte with 0.1 M NaCl and 5 mM $HAuCl_4$[47]. The pure Au catalyst was prepared *via* the similar electrodeposition method by directly using Ni foam as the working electrode.

Preparation of Au/CoOOH: The *Au/CoOOH* was obtained from the as-prepared $Au/Co(OH)_2$ *via* a simple cyclic voltammetry (CV) method in a three-electrode configuration, using Ag/AgCl (with saturated KCl) and Pt foil as the reference and counter electrodes respectively. The electrochemical oxidization process was performed at a scan rate of 100 mV s^{-1} from 0 V to 0.8 V *vs*. Ag/AgCl for approximately 20 cycles in 1 M KOH solution[46]. The pure CoOOH catalyst was prepared *via* the similar electrochemical oxidization method by using as-obtained $Co(OH)_2$ as the working electrode.

Characterizations

X-ray diffraction patterns were collected on a Shimadzu XRD-6000 diffractometer using a Cu Kα source, with a scan range of 3–70° and scan step of 5° min^{-1}. X-ray photoelectron spectra (XPS) were performed on a Thermo VG ESCALAB 250 X-ray photoelectron spectrometer at a pressure of about 2×10^{-9} Pa using Al Kα X-rays as the excitation source. Scanning electrode microscope (SEM) imaging was performed using a Zeiss SUPRA 55 Field Emission SEM with an accelerating voltage of 20 kV. Transmission electron microscopy (TEM) images were recorded with JEOL JEM-2010 high resolution (HR-) TEM with an accelerating voltage of 200 kV, combined with energy dispersive X-ray spectroscopy (EDX) for the determination of metal composition. Metal contents in

catalysts were determined by ICP-AES on a Thermo ICAP6300 Radial. The operando Au and Co XAFS measurements was performed at the beamline 1W1B of the Beijing Synchrotron Radiation Facility (BSRF), Institute of High Energy Physics (IHEP), Chinese Academy of Sciences (CAS). Extended X-ray absorption fine structure spectra (EXAFS) were recorded at ambient temperature in transmission mode. The typical energy of the storage ring was 2.5 GeV with a maximum current of 250 mA; the Si (111) double crystal monochromator was used. Fourier transform of the EXAFS spectra were carried out in a *K*-range from 3.0 to 12.8 $Å^{-1}$. The *in-situ* FTIR spectra of benzyl alcohol were carried out in a Bruker Equinox 55 spectrometer, between 4000 and 400 cm^{-1} with a resolution of 4 cm^{-1} after 600 scans per spectrum. About 30 mg of the sample was pressed into a wafer with a diameter of 13 mm, which was then installed in an *in-situ* IR reactor with CaF_2 windows. The sample was pre-processing by He gas at r.t. for 1 h and then benzyl alcohol was flowed into the cell for 30 min, then physically adsorbed benzyl alcohol was removed by flowing He gas for 30 min. The FTIR spectra were *in-situ* collected during the He purging process[38].

Electrochemical measurement

All electrochemical measurements for alcohols oxidation were performed in 1 M KOH electrolyte at r.t. or 60 ºC on an electrochemical workstation (CHI 760E, CH Instruments, Inc.). The electrochemical tests were performed in a three-electrode system, using Ag/AgCl electrode (with saturated KCl) and Pt foil as reference and counter electrode, respectively. Linear scan voltammetry (LSV) curves of catalysts were acquired from −0.2 V to 0.6 V *vs.* Ag/AgCl at a scan rate of 10 mV s^{-1}. All potentials measured against Ag/AgCl were converted to the reversible hydrogen electrode (RHE) scale using: $E\ vs.\ \mathrm{RHE} = E\ vs.\ \mathrm{Ag/AgCl} + 0.197 + 0.059\mathrm{pH}$. The detailed energy balance calculations were also conducted to analyse the consumption of electric energy. The value of electric energy was determined using: $W_E = U \times I \times t$ [16]. . The space-time yield of H_2 in Fig. 2d was obtained by gas-collecting method of drainage water. For long-term electrochemical measurement by intermittent potential (IP) and constant potential (CP) strategies, the productivity of H_2 (in Fig. 6b) was calculated based on the charge transfer of benzyl alcohol oxidation. The aromatic alcohols, aldehydes, and acids were quantified by high performance liquid chromatography (HPLC; Angilent 1200 Infinity Series) equipped with C18 column (Cosmosil C18-MS-II) using MeCN/H_2O/H_3PO_4 (40/60/0.05) as mobile phase and detected by UV detector at 220 nm. Aliphatic alcohols, aldehydes, and acids were quantified by HPLC equipped with organic acid column (Coregel 87H3) using 5 mM aqueous H_2SO_4 as mobile phase and detected by UV detector (210 nm) and refractive index detector.

Computational details

Model construction of CoOOH, Au, and Au/CoOOH: In total, three models (denoted as CoOOH, Au, and Au/CoOOH) were constructed to represent CoOOH surface, Au surface

and Au/CoOOH interface in Au/CoOOH, respectively.

The model of bulk γ-CoOOH was built according to the experimental X-ray diffraction pattern[48]. The space group of bulk γ-CoOOH was R mH, with the lattice parameters of $a = b = 2.82$ Å, $c = 20.65$ Å, $\alpha = \beta = 90º$, $\gamma = 120º$. After that, the model of CoOOH was built by cleaving the (001) facet of bulk γ-CoOOH since the (001) facet was the preferably exposed facet according to the X-ray diffraction pattern. The model CoOOH contained one layer of Co and H atoms, and two layers of O atoms, together with a vacuum layer of 15 Å. Thus, the chemical formula of CoOOH was $Co_{16}O_{32}H_{16}$.

The model of bulk Au was built according to the experimental X-ray diffraction pattern[49]. The space group of bulk Au was Fm m, with the lattice parameters of $a = b = c = 4.07$ Å, $\alpha = \beta = \gamma = 90º$. In previous literature, the (111) facet had been widely reported to be the preferably exposed facet of bulk Au[50]. Thus, the model of Au was built by cleaving the (111) facet of bulk Au. The model Au contained four layers of Au atoms, and a vacuum layer of 15 Å. Thus, the chemical formula of model Au was Au_{36}.

The model of Au/CoOOH was built in three steps. Firstly, the (001) facet of CoOOH was cleaved with the supercell of 8 × 8 in the *a*-, and *b*- directions. Secondly, a close-packed Au cluster was cleaved according to the (111) facet of bulk Au. This Au_{37} cluster contained 19, 12, and 6 Au atoms in the bottom, middle, and uppermost layers. At last, the model of Au/CoOOH was built by putting the Au_{37} cluster on the CoOOH (001) facet. Both CoOOH (001) and Au (111) facets were exposed in this Au/CoOOH model, therefore this model could well represent the catalyst used in the experiment.

In calculating the mechanism of benzyl alcohol oxidation to benzoic acid on catalyst, the models of Ph-CH_2OH*, Ph-CHOH*, Ph-CH_2O*, Ph-CHO*, Ph-$CH(OH)_2$*, Ph-$C(OH)_2$*, Ph-CHOOH*, and Ph-COOH* (* denoted the adsorption site) were constructed with corresponding intermediates adsorbed on the adsorption site.

In order to simulate the adsorption behaviors of benzyl alcohol on CoOOH, or Au/CoOOH in real reaction system, the models of CoOOH_sol, and Au/CoOOH_sol were built by adding the water solvent of 1.0 g cm^{-3} and four benzyl alcohol molecules into the vacuum layer of CoOOH or Au/CoOOH.

Computational methods: The spin-polarized density functional theory (DFT) calculations at the generalized gradient approximation (GGA) Perdew-Burke-Ernzerhof (PBE) level[51] were performed with the Cambridge Sequential Total Energy Package (CASTEP)[52]. The ionic cores were described by the ultrasoft pseudopotentials to decrease the number of plane waves required in the expansion of the Kohn-Sham orbitals[53]. The cutoff energy was set as 380 eV. The Broyden-Fletcher-Goldfarb-Shanno (BFGS) algorithm was used to search the potential energy surface in geometry optimization[54]. The *k*-point meshes were set as 3 × 3 × 1. During the geometry optimization, three convergence criteria were used as follows:

(1) energy tolerance of 1.0×10^{-5} eV per atom, (2) force tolerance of 3.0×10^{-2} eV/Å, (3) displacement tolerance of 1.0×10^{-3} Å.

The *ab initio* molecular dynamics (AIMD) simulations were performed in isothermal-isobaric (*NPT*) ensemble, with a temperature of 298.15 K and a pressure of 0.1 MPa. The temperature and pressure were controlled by the Nose method[55], and Andersen method[56], respectively. The total simulation time of 1000 ps was performed for both CoOOH_sol and Au/CoOOH_sol with a time step of 1 fs.

The adsorption energy of benzyl alcohol was calculated with eq 1:

$$E_{ads} = E_{Ph\text{-}CH_2OH^*} - E_* - E_{Ph\text{-}CH_2OH} \quad (1)$$

where E_{ads}, $E_{Ph\text{-}CH_2OH^*}$, E_*, and $E_{Ph\text{-}CH_2OH}$ represented the adsorption energy of benzyl alcohol, energy of Ph-CH_2OH*, *, and benzyl alcohol, respectively. The oxidation of benzyl alcohol to benzoic acid happened in seven consecutive steps:

$$* + Ph\text{-}CH_2OH \rightarrow Ph\text{-}CH_2OH^* \quad (A)$$

$$Ph\text{-}CH_2OH^* + OH^- \rightarrow Ph\text{-}CHOH^*/Ph\text{-}CH_2O^* + H_2O + e^- \quad (B)$$

$$Ph\text{-}CHOH^*/Ph\text{-}CH_2O^* + OH^- \rightarrow Ph\text{-}CHO^* + H_2O + e^- \quad (C)$$

$$Ph\text{-}CHO^* + H_2O \rightarrow Ph\text{-}CH(OH)_2^* \quad (D)$$

$$Ph\text{-}CH(OH)_2^* + OH^- \rightarrow Ph\text{-}C(OH)_2^*/Ph\text{-}CHOOH^* + H_2O + e^- \quad (E)$$

$$Ph\text{-}C(OH)_2^*/Ph\text{-}CHOOH^* + OH^- \rightarrow Ph\text{-}COOH^* + H_2O + e^- \quad (F)$$

$$Ph\text{-}COOH^* \rightarrow * + Ph\text{-}COOH \quad (G)$$

Among them, the steps A and G were the adsorption of benzyl alcohol and desorption of benzoic acid, respectively. The step D was the spontaneous hydration of benzaldehyde. The other four steps were the oxidative step with one electron transfer. The Gibbs free energy change (ΔG) of each elementary step was calculated by minus the Gibbs free energy of reactant from that of the product. The Gibbs free energy was obtained by calculating the phonon density of states, as shown in eq 2:

$$G = E + ZPE + kT\int F(\omega)\ln[1-\exp(-\frac{\hbar\omega}{kT})]d\omega \quad (2)$$

where E was the total energy, ZPE was the zero-point energy, the term $kT\int F(\omega)\ln[1-\exp(-\frac{\hbar\omega}{kT})]d\omega$ was the correction of Gibbs free energy *via* thermodynamics analysis.

The electronic structures of benzyl alcohol, methallyl alcohol, and hydroxyacetone were calculated at the B3LYP level[57] in the Gaussian 09 program[58].

Data Availability

The data that support the plots within the manuscript and other findings of this study are available from the corresponding author upon reasonable request.

References

1. Wu, T. <bi>et al.</bi> **Iron-facilitated dynamic active-site generation on spinel $CoAl_2O_4$ with self-termination of surface reconstruction for water oxidation**. *Nat. Catal.* **2**, **763–772** (2019).
2. Kibsgaard, J. & Chorkendorff, I. **Considerations for the scaling-up of water splitting catalysts**. *Nat. Energy* **4**, **430–433** (2019).
3. Suntivich, J., May, K. J., Gasteiger, H. A., Goodenough, J. B. & **Shao-Horn, Y. A perovskite oxide optimized for oxygen evolution catalysis from molecular orbital principles**. *Science* **334**, **1383–1385** (2011).
4. Chen, Z. <bi>et al.</bi> **Boride-based electrocatalysts: Emerging candidates for water splitting**. *Nano Res.* **13**, **293–314** (2020).
5. Du, L. <bi>et al.</bi> **Electrocatalytic valorisation of biomass derived chemicals**. *Catal. Sci. Technol.* **8**, **3216 – 3232** (2018).
6. Chen, Y. X. <bi>et al.</bi> **Nanotechnology makes biomass electrolysis more energy efficient than water electrolysis**. *Nat. Commun.* **5**, **4036** (2014).
7. Leow, W. R. <bi>et al.</bi> **Chloride-mediated selective electrosynthesis of ethylene and propylene oxides at high current density**. *Science* **368**, **1228–1233** (2020).
8. Zheng, J. <bi>et al.</bi> **Hierarchical porous NC@CuCo nitride nanosheet networks: highly efficient bifunctional electrocatalyst for overall water splitting and selective electrooxidation of benzyl alcohol**. *Adv. Funct. Mater.* **27**, **1704169** (2017).
9. Sherbo, R. S. <bi>et al.</bi> **Complete electron economy by pairing electrolysis with hydrogenation**. *Nat. Catal.* **1**, **501–507** (2018).
10. Li, W. <bi>et al.</bi> **Electrolyzer design for flexible decoupled water splitting and organic upgrading with electron reservoirs**. *Chem* **4**, **637–649** (2018).
11. You, B., Liu, X., Jiang, N. & Sun, Y. **A general strategy for decoupled hydrogen production from water splitting by integrating oxidative biomass valorization**. *J. Am. Chem. Soc.* **138**, **13639 – 13646** (2016).
12. Huang, Y., Chong, X., Liu, C., Liang, Y. & Zhang, B. **Boosting hydrogen production by anodic oxidation of primary amines over a NiSe nanorod electrode**. *Angew. Chem. Int. Ed.* **57**, **13163 – 13166** (2018).
13. Huang, C., Huang, Y., Liu, C., Yu, Y. & Zhang, B. **Integrating hydrogen production with aqueous selective semi-dehydrogenation of tetrahydroisoquinolines over a Ni_2P bifunctional electrode**. *Angew. Chem. Int. Ed.* **58**, **12014 – 12017** (2019).
14. Verma, S., Lu, S. & Kenis, P. J. A. **Co-electrolysis of CO_2 and glycerol as a pathway to carbon chemicals with improved technoeconomics due to low electricity consumption**. *Nat. Energy* **4**, **466–474** (2019).
15. Huang, H. <bi>et al.</bi> Ni, **Co hydroxide triggers electrocatalytic production of high-purity benzoic acid over 400 mA cm^{-2}**. *Energy Environ. Sci.*<bi>,</bi> **doi**: 10.1039/D0EE02607G (2020).

16. Li, Y., Wei, X., Chen, L., Shi, J. & He, M. **Nickel-molybdenum nitride nanoplate electrocatalysts for concurrent electrolytic hydrogen and formate productions**. *Nat. Commun.* **10**, **5335** (2019).
17. Dai, C. <bi>et al.</bi> **Electrochemical production of lactic acid from glycerol oxidation catalyzed by AuPt nanoparticles**. *J. Catal.* **356**, **14–21** (2017).
18. Liu, W.-J. <bi>et al.</bi> **Efficient electrochemical production of glucaric acid and H_2 *via* glucose electrolysis**. *Nat. Commun.* **11**, **265** (2020).
19. Li, F. <bi>et al.</bi> **Cooperative CO_2-to-ethanol conversion via enriched intermediates at molecule–metal catalyst interfaces**. *Nat. Catal.* **3**, **75–82** (2020).
20. Nam, D. H. <bi>et al.</bi> **Molecular enhancement of heterogeneous CO_2 reduction**. *Nat. Mater.* **19**, **266–276** (2020).
21. Gao, W. <bi>et al.</bi> **Industrial carbon dioxide capture and utilization: state of the art and future challenges**. *Chem. Soc. Rev.* **doi**: 10.1039/D0CS00025F (2020).
22. Huang, J. <bi>et al.</bi> **CoOOH nanosheets with high mass activity for water oxidation**. *Angew. Chem. Int. Ed.* **20**, **8846 – 8851** (2015).
23. Dionigi, F. <bi>et al. In-situ</bi> **structure and catalytic mechanism of NiFe and CoFe layered double hydroxides during oxygen evolution**. <bi>Nat. Commun.</bi> **11**, **2522** (2020).
24. Yin, Z. <bi>et al.</bi> **Engineering interface with one-dimensional Co_3O_4 nanostructure in catalytic membrane electrode: toward an advanced electrocatalyst for alcohol oxidation**. *ACS Nano* **11**, **12365 – 12377** (2017).
25. Xu, Y. <bi>et al.</bi> **Highly active zigzag-like Pt-Zn alloy nanowires with high-index facets for alcohol electrooxidation**. *Nano Res.* **12**, **1173–1179** (2019).
26. Ureta-Zañartu, M. S. <bi>et al.</bi> **Electrocatalytic oxidation of alcohols at gold electrodes in alkaline media**. *Int. J. Electrochem. Sci.* **7**, **8905–8928** (2012).
27. Zhou, C. <bi>et al.</bi> **Promoting role of bismuth on carbon nanotube supported platinum catalysts in aqueous phase aerobic oxidation of benzyl alcohol**. *Appl. Catal. B: Environ.* **181**, **118–126** (2016).
28. Souto, R. M., Rodríguez, J. L., Pastor, E. & Iwasita, T. **Spectroscopic investigation of the adsorbates of benzyl alcohol on palladium**. *Langmuir* **16**, **8456–8462** (2000).
29. Lu, Y. <bi>et al.</bi> **Identifying the geometric site dependence of spinel oxides for the electrooxidation of 5-hydroxymethylfurfural**. *Angew. Chem. Int. Ed.* **59**, **19215 – 19221** (2020).
30. Liu, Z., Zhang, C., Liu, H. & Feng, L. **Efficient synergism of $NiSe_2$ nanoparticle/NiO nanosheet for energyrelevant water and urea electrocatalysis**. *Appl. Catal. B: Environ.* **276**, **119165** (2020).
31. Liu, W.-J.<bi>, et al.</bi> **Electrochemical oxidation of 5–hydroxymethylfurfural with NiFe layered double hydroxide (LDH) nanosheet catalysts**. *ACS Catal*<bi>.</bi> **8**, **5533 – 5541** (2018).
32. Nam, D.-H., Taitt, B. J. & Choi, K.-S. **Copper-based catalytic anodes to produce 2,5-furandicarboxylic acid, a biomass-drived alternative to terephthalic acid**. *ACS Catal*<bi>.</bi> **8**, **1197 – 1206** (2018).
33. Zhang, N. <bi>et al.</bi> **Electrochemical oxidation of 5-hydroxymethylfurfural on nickel nitride/carbon nanosheets: reaction pathway determined by in situ sum frequency generation**

vibrational spectroscopy. *Angew. Chem. Int. Ed.* **58**, **15895 – 15903** (2019).

34. Zhu, X. <bi>et al.</bi> **Metallic nickel hydroxide nanosheets give superior electrocatalytic oxidation of urea for fuel cells**. *Angew. Chem. Int. Ed.* **55**, **12465 – 12469** (2016).
35. Villa, A. <bi>et al.</bi> **Operando attenuated total reflectance FTIR spectroscopy: studies on the different selectivity observed in benzyl alcohol oxidation.** *ChemCatChem* **7**, **2534–2541** (2015).
36. Zou, J. <bi>et al.</bi> **Photocatalytic selective oxidation of benzyl alcohol over ZnTi-LDH: The effect of surface OH groups**. *Appl. Catal. B: Environ.* **260**, **118185** (2020).
37. Zhang, X., Ke, X. & Zhu, H. **Zeolite-supported gold nanoparticles for selective photooxidation of aromatic alcohols under visible-light irradiation**. *Chem. Eur. J.* **18**, **8048–8056** (2012).
38. Luo, L. <bi>et al</bi>. **Selective activation of benzyl alcohol coupled with photoelectrochemical water oxidation via a radical relay strategy**. *ACS Catal.* **10**, **4906–4913** (2020).
39. Awate, S. V., Sahu, R. K., Kadgaonkar, D. M. Kumar, R. & Gupta, N. M. **Photocatalytic mineralization of benzene over gold containing titania nanotubes: Role of adsorbed water and nanosize gold crystallites**. *Catal. Today* **141**, **144–151** (2009).
40. Liang, S. <bi>et al.</bi> **Monolayer HNb_3O_8 for selective photocatalytic oxidation of benzylic alcohols with visible light response**. *Angew. Chem. Int. Ed.* **53**, **2951 – 2955** (2014).
41. Li, H. <bi>et al.</bi> **New reaction pathway induced by plasmon for selective benzyl alcohol oxidation on BiOCl possessing oxygen vacancies**. *J. Am. Chem. Soc.* **139**, **3513 – 3521** (2017).
42. Shishido, T. <bi>et al.</bi> **Mechanism of photooxidation of alcohol over Nb_2O_5**. *J. Phys. Chem. C* **113**, **18713–18718** (2009).
43. Zhao, X., Wang, P., Ma, Z. & Pei, Y. **Phenyl ring transfer mechanism of styrene selective oxidation to phenyl acetaldehyde on gold catalysts from density functional theory (DFT) studies**. *J. Phys. Chem. C* **123**, **1710 – 1719** (2019).
44. Wang, Y., Ren, J., Deng, K., Gui, L. & Tang, Y. **Preparation of tractable platinum, rhodium, and ruthenium nanoclusters with small particle size in organic media.** *Chem. Mater.* **12**, **1622–1627** (2000).
45. Ishida, T., Murayama, T., Taketoshi, A. & Haruta, M. **Importance of size and contact structure of gold nanoparticles for the genesis of unique catalytic processes**. *Chem. Rev.* **120**, **464–525** (2020).
46. Li, Z. <bi>et al</bi>. **Ordered-vacancy-induced cation intercalation into layered double hydroxides: a general approach for high-performance supercapacitors**. *Chem.* **4**, **2168–2179** (2018).
47. Zhang, J. <bi>et al</bi>. **Single-atom Au/NiFe layered double hydroxide electrocatalyst: probing the origin of activity for oxygen evolution reaction**. *J. Am. Chem. Soc.* **140**, **3876 – 3879** (2018).
48. Glemser, O. & Einerhand, J. **Die struktur hoherer nickel hydroxyde locality: synthetic**. *Z. Anorg. Allg. Chem.* **261**, **43 – 51** (1950).
49. Spreadborough, J. & Christian, J. W. **High-temperature X-ray diffractometer**. *J. Sci. Instrum.* **36**, **116 – 118** (1959).

50. Barth, J. V., Brune, H., Ertl, G. & Behm, R. J. **Scanning tunneling microscopy observations on the reconstructed gold (111) surface: atomic structure, long-range superstructure, rotational domains, and surface defects**. *Phys. Rev. B* **42**, **9307 – 9318 (**1990**)**.
51. Perdew, J. P., Burke, K. & Ernzerhof, M. **Generalized gradient approximation made simple**. *Phys. Rev. Lett.* **77**, **3865 – 3868 (**1996**)**.
52. Clark, S. J. <bi>et al</bi>. **First principles methods using CASTEP**. *Zeitschrift Fur. Kristallographie* **220**, **567 – 570 (**2005**)**.
53. Vanderbilt, D. **Soft self-consistent pseudopotentials in a generalized eigenvalue formalism**. *Phys. Rev. B* **41**, **7892 – 7895 (**1990**)**.
54. Anglada, J. M. & Bofill, J. M. **How good is a Broyden-Fletcher-Goldfarb-Shanno-like update Hessian formula to locate transition structure? Specific reformulation of Broyden-Fletcher-Goldfarb-Shanno for optimizing saddle points**. *J. Comput. Chem.* **19**, **349 – 362 (**1998**)**.
55. Nose, S. **A molecular dynamics method for simulations in the canonical ensemble**. *J. Chem. Phys.* **135**, **164111 (**2011**)**.
56. Andersen, H. C. **Molecular dynamics simulations at constant pressure and/or temperature**. *J. Chem. Phys.* **72**, **2384 – 2393 (**1980**)**.
57. Lee, C., Yang, W. & Parr, R. G. **Development of the Colle-Salvetti correlation-energy formula into a functional of the electron density**. *Phys. Rev. B* **37**, **785 – 789 (**1988**)**.
58. Frisch, M. J. <bi>et al</bi>. **Gaussian 09**, **Revision A.02** (**Gaussian Inc**, 2009).

Declarations

Acknowledgements

This work was supported by the National Natural Science Foundation of China (Grant No. 21978147, 21935001, 21991102). The authors thank the BL1W1B in the Beijing Synchrotron Radiation Facility (BSRF).

Author Contributions

Z.L. designed and carried out the synthesis, characterizations and catalytic reactions, analyzed the data and wrote the manuscript. S.X. performed DFT calculations and AIMD simulations. Y.Y. and H.Z. carried out catalytic reactions and analyzed the data. M.X., B.W. and L.Z. performed *in situ* EXAFS and FTIR measurements and analyzed the data. L.M. and X.K. regulated the experiments and anticipated discussion. H.D. supervised the project, conceived the idea, helped design the experiments, analyzed the data and wrote the manuscript. All the authors commented on the manuscript and have given approval to the final version of the manuscript.

Additional information

Supplementary Information is available in the online version of the paper. Reprints and permissions information is available online at www.nature.com/reprints. Correspondence should be addressed to H.D.

Competing interests

The authors declare no competing interests.

Figures

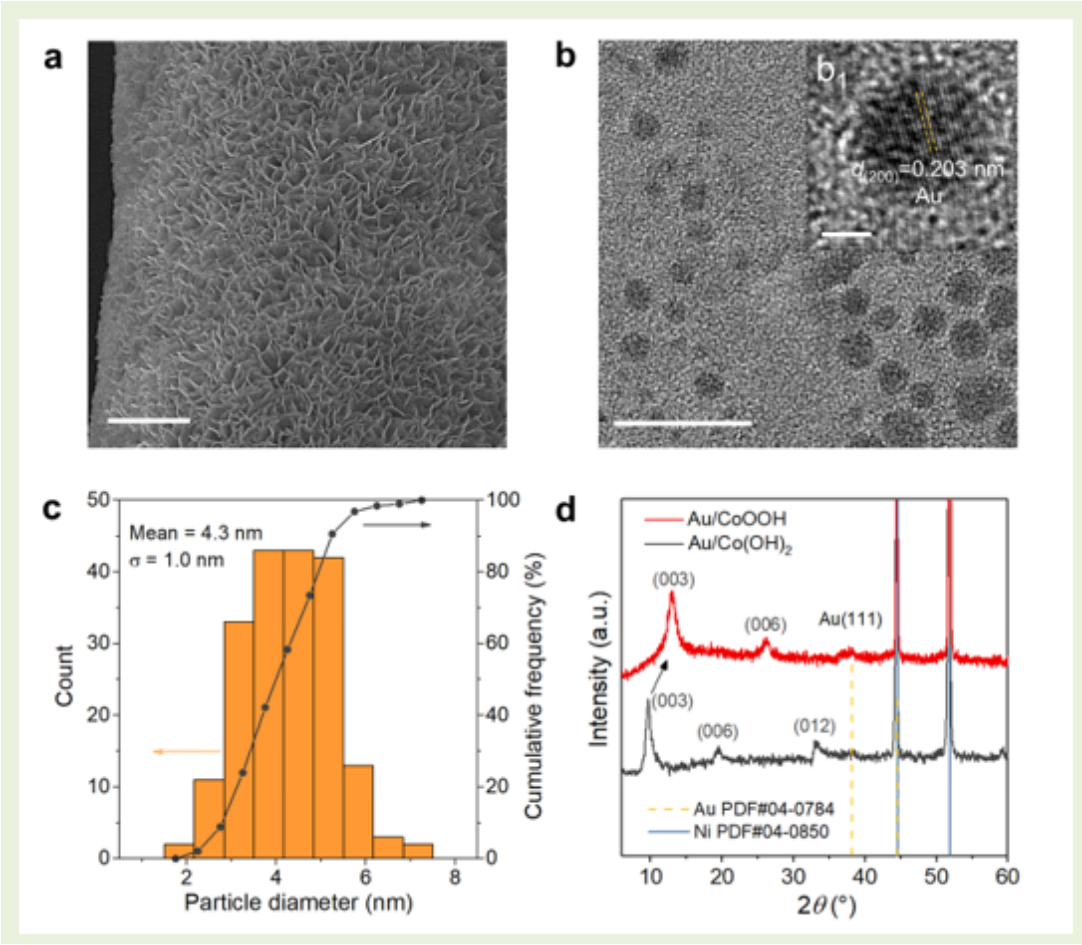

Figure 1

Structural characterization of the Au/CoOOH catalyst. a, SEM image of the Au/CoOOH catalyst. Scale bar, 3 μm. b, HRTEM images of a representative region. Inset displays an individual Au nanoparticle. Scale bars: 20 nm (b); 2 nm (inset). c, Size distribution of the Au nanoparticles. d, XRD patterns of the Au/CoOOH catalyst and Au/Co(OH)2.

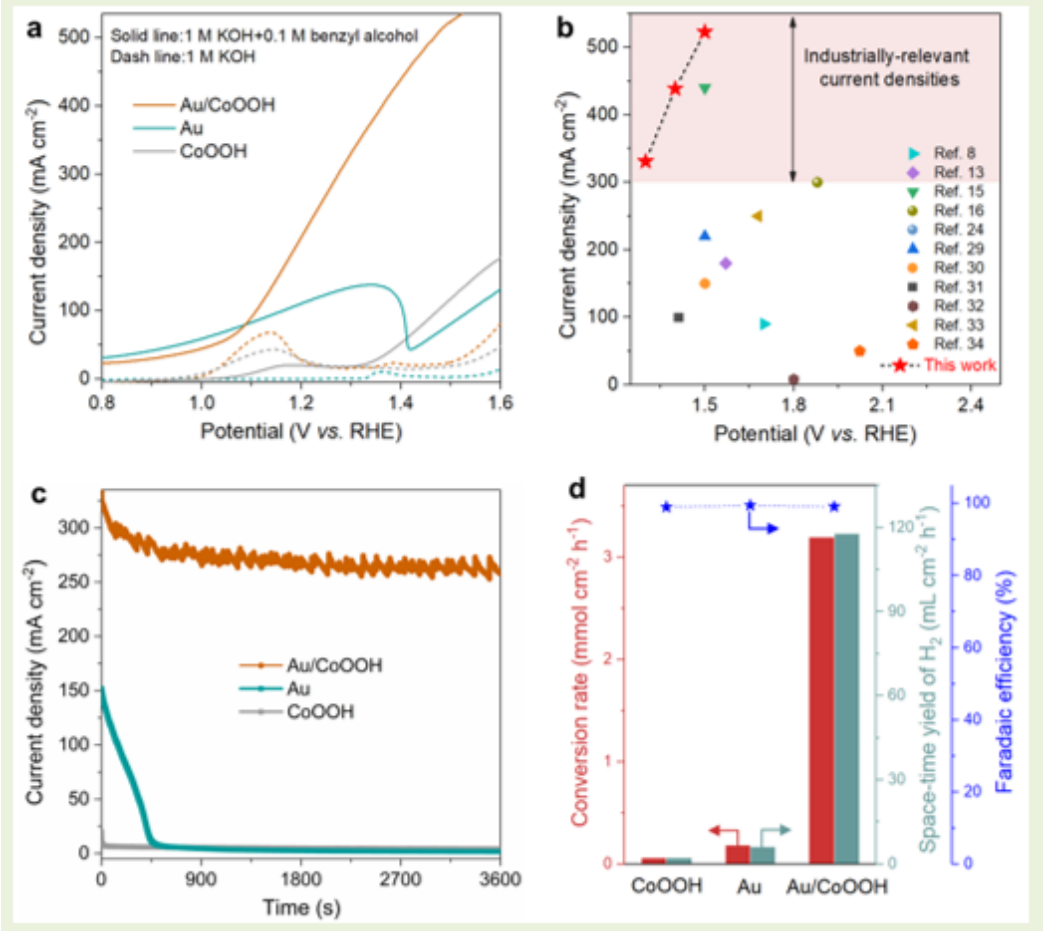

Figure 2

Au/CoOOH catalyst for benzyl alcohol electrooxidation. a, LSV curves at scan rate of 10 mV s−1 in 1 M KOH with 0.1 M benzyl alcohol at r.t. over different anodes. b, Current densities of anodic oxidation reactions reported in the literatures and the benzyl alcohol oxidation in this work. Comparison of c, I-t curves and d, benzyl alcohol conversion rate, H2 space-time yield and faradaic efficiency over different anodes coupled Pt cathode, in 1 M KOH with 0.1 M benzyl alcohol at 1.3 V vs. RHE.

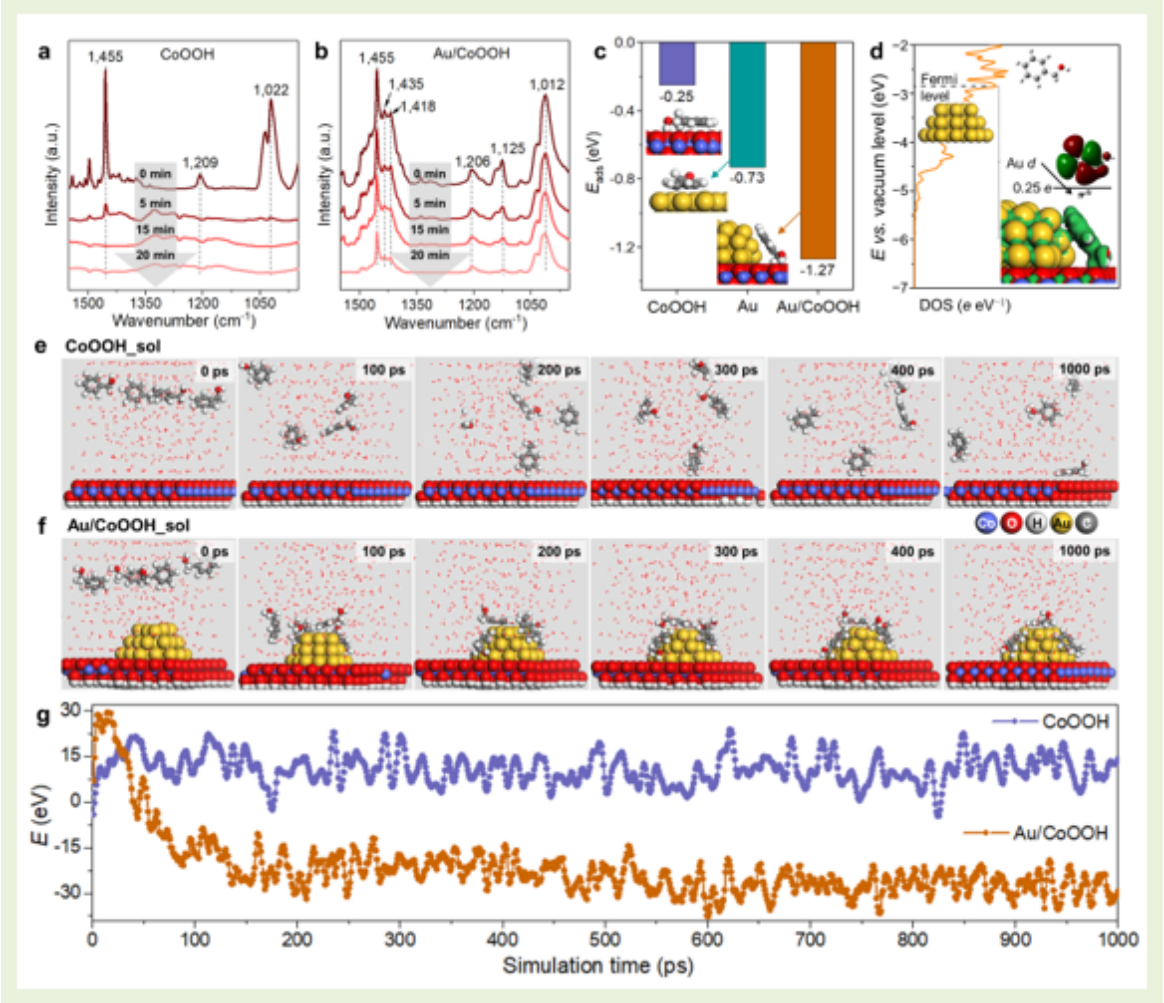

Figure 3

Mechanistic investigation of benzyl alcohol enrichment. a, FTIR spectra of CoOOH after benzyl alcohol adsorption. b, FTIR spectra of Au/CoOOH after benzyl alcohol adsorption. c, Adsorption energies of benzyl alcohol on CoOOH, Au, and Au/CoOOH, the optimized geometries of Ph-CH2OH* are also displayed. d, Partial density of states for Au-d orbital in Au/CoOOH, together with the energy level of π* orbital in benzyl alcohol. The isosurface of Ph-CH2OH* is also displayed. e, Snapshots of CoOOH_sol at AIMD simulation time of 0, 100, 200, 300, 400, and 1000 ps. f, Snapshots of Au/CoOOH_sol at AIMD simulation time of 0, 100, 200, 300, 400, and 1000 ps. g, Energy evolution of CoOOH_sol and Au/CoOOH_sol during AIMD simulations.

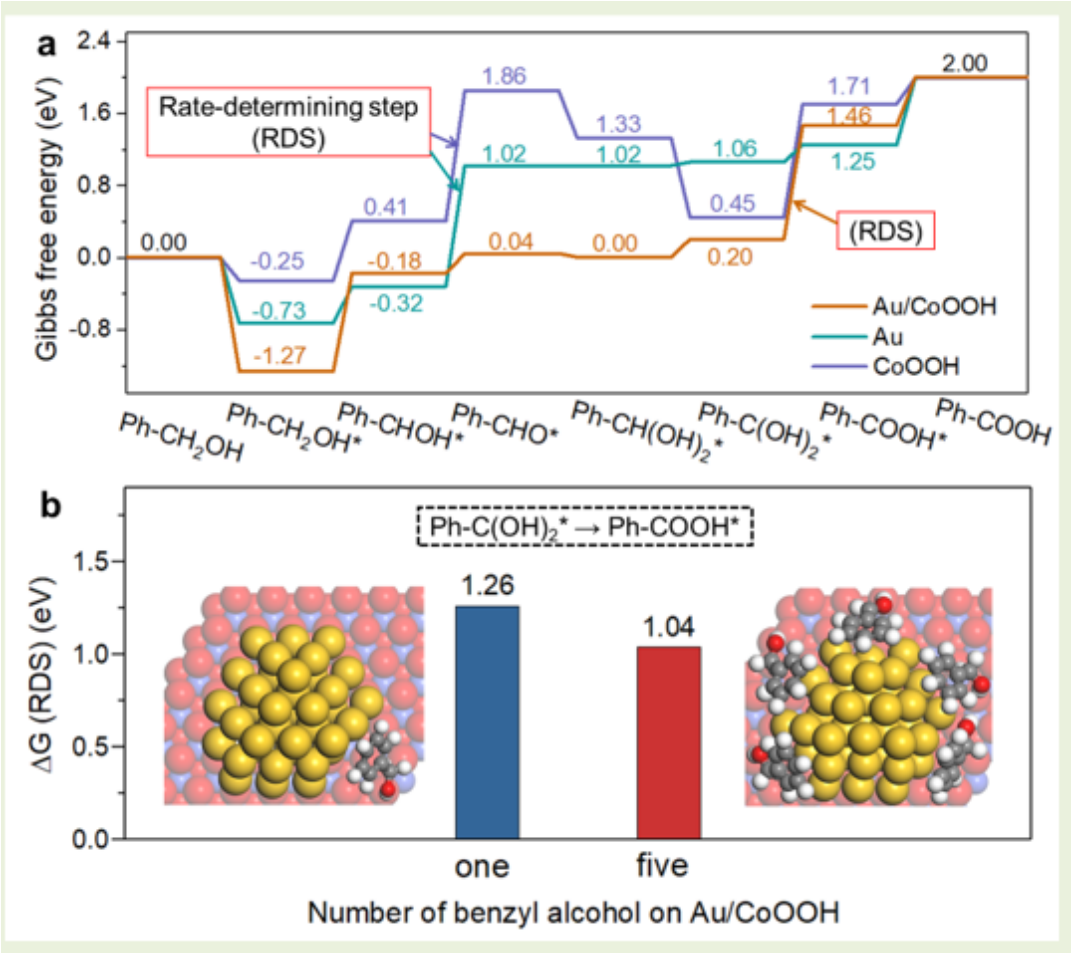

Figure 4

Reaction mechanism of benzyl alcohol oxidation. a, Gibbs free energy diagrams of benzyl alcohol oxidation to benzoic acid on CoOOH, Au, and Au/CoOOH. b, ΔG of RDS for benzyl oxidation on Au/CoOOH with one and five benzyl alcohol molecules adsorption, respectively. Inset displays the associated optimized geometries.

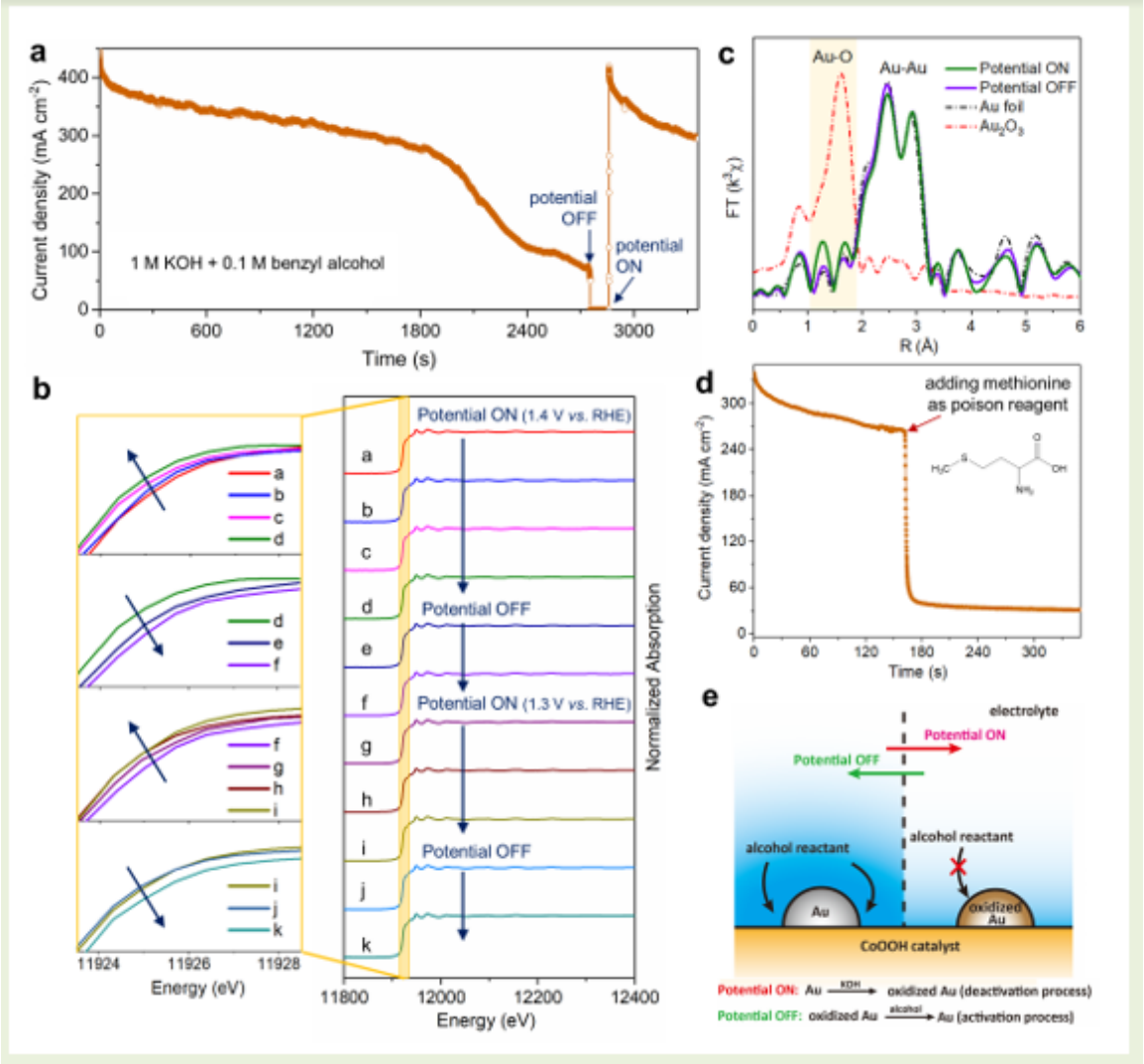

Figure 5

Mechanism of the decay and revival of current density over Au/CoOOH catalyst. a, I-t curve of Au/CoOOH catalyst at 1.4 V vs. RHE in 1 M KOH with 0.1 M benzyl alcohol at r.t. b, Au L3-edge XANES spectra of Au/CoOOH between anodic potential and open circuit in 1 M KOH with 0.1 M benzyl alcohol at r.t. c, Fourier-transform Au L3-edge EXAFS spectra of Au/CoOOH, Au foil and Au2O3. d, I-t curve of Au/CoOOH at 1.3 V vs. RHE in 1 M KOH with 0.1 M benzyl alcohol at r.t. (methionine was added at 160 s). e, Schematic illustration of reversible oxidation and reduction of Au for alcohol enrichment.

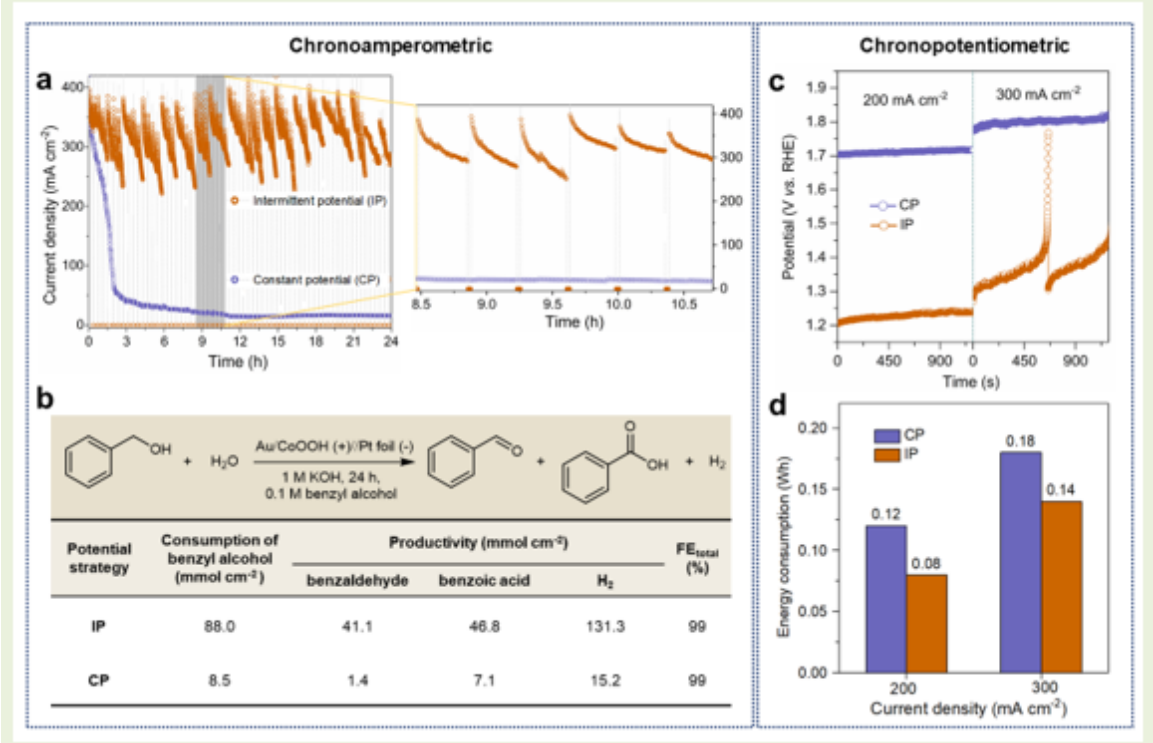

Potential strategy	Consumption of benzyl alcohol (mmol cm^{-2})	Productivity (mmol cm^{-2})			FE_{total} (%)
		benzaldehyde	benzoic acid	H_2	
IP	88.0	41.1	46.8	131.3	99
CP	8.5	1.4	7.1	15.2	99

Figure 6

Long-term enrichment of alcohols for enhanced electrooxidation. a, Chronoamperometric measurements of Au/CoOOH catalyst using intermittent potential (IP) and constant potential (CP) strategies at 1.35 V vs. RHE in 1 M KOH with 0.1 M benzyl alcohol at r.t. over 24 h (left), and enlarged measurement period in a (right). b, The corresponding consumption of benzyl alcohol, productivities of benzaldehyde, benzoic acid and H2, as well as the FE of total anodic products. c, Chronopotentiometric measurements of Au/CoOOH catalyst with IP and CP strategies at 150 and 250 mA cm−2 in 1 M KOH with 0.1 M benzyl alcohol at r.t. d, The corresponding electric energy consumption.

Supplementary Files

This is a list of supplementary files associated with this preprint. Click to download.

- SupplementaryInformation20201201HD.docx
- Supplementaryvideo1.mp4
- Supplementaryvideo2.mp4
- Table1.docx
- Scheme1.docx